Robotica (2017) volume 35, pp. 1310–1326. © Cambridge University Press 2016
doi:10.1017/S0263574716000059

Stiffness analysis and comparison of a Biglide parallel grinder with alternative spatial modular parallelograms

Guanglei Wu†* and Ping Zou‡

†*Department of Mechanical and Manufacturing Engineering, Aalborg University, 9220 Aalborg, Denmark*
‡*School of Mechanical Engineering and Automation, Northeastern University, 110819 Shenyang, P. R. China. E-mail: pzou@mail.neu.edu.cn*

(Accepted January 13, 2016. First published online: February 8, 2016)

SUMMARY
This paper deals with the stiffness modeling, analysis and comparison of a Biglide parallel grinder with two alternative modular parallelograms. It turns out that the Cartesian stiffness matrix of the manipulator has the property that it can be decoupled into two homogeneous matrices, corresponding to the translational and rotational aspects, through which the principal stiffnesses and the associated directions are identified by means of the eigenvalue problem, allowing the evaluation of the translational and rotational stiffness of the manipulator either at a given pose or the overall workspace. The stiffness comparison of the two alternative Biglide machines reveals the (dis)advantages of the two different spatial modular parallelograms.

KEYWORDS: Biglide parallel grinder; Parallelogram; Stiffness decoupling; Principal stiffness.

1. Introduction

Parallel manipulators (PMs) have found their applications in many fields, thanks to their advantages in terms of simple structure, low inertia, high structural stiffness and high accuracy. etc.[1] Amongst the applications, one major application is that they can function as a machine tool for material processing, where the stiffness behavior is of importance as the stiffness strongly influences the positioning and orientation accuracies in the stages of design and applications. In this paper, a parallel Biglide mechanism based grinder is to be investigated.

The manipulator stiffness is usually characterized with its stiffness matrix, which maps the transformation between the translational/rotational deformations and the external wrench in the Cartesian space. A commonly used approach to model the stiffness matrix of PMs is the Virtual Joint Method (VJM), i.e., the lumped modeling, since it provides acceptable accuracy in short computational time. Gosselin[2] was the first to apply the VJM approach to the PMs, in which only the actuation compliance described by one-dimensional linear springs were considered while both the links and the passive joints were assumed to be rigid. Later on, the external loads, which cause the changes in the Jacobian, namely, the robot geometry change, were taken into account in the stiffness modeling.[3,4] Quennouelle and Gosselin[5] also investigated the conservative property of the stiffness matrix with the consideration of the external loads and firstly considered the influence of the passive joints. Generally, the link flexibilities have been taken into account during the development of the VJM approach, where the link is simplified as a flexible-link lumped parametric model.[6–8] Combining the advantages of the foregoing approaches, Pashkevich *et al.* proposed a stiffness modeling method named as virtual spring approach, which can be applied to the manipulator at both unloaded equilibrium condition[9] and loaded case.[10] In this approach, the link flexibility is replaced by localizing a n-dofs virtual spring that is associated with the mobilities describing both the translational and rotational deflections and

* Corresponding author. E-mail: gwu@m-tech.aau.dk

https://doi.org/10.1017/S0263574716000059 Published online by Cambridge University Press

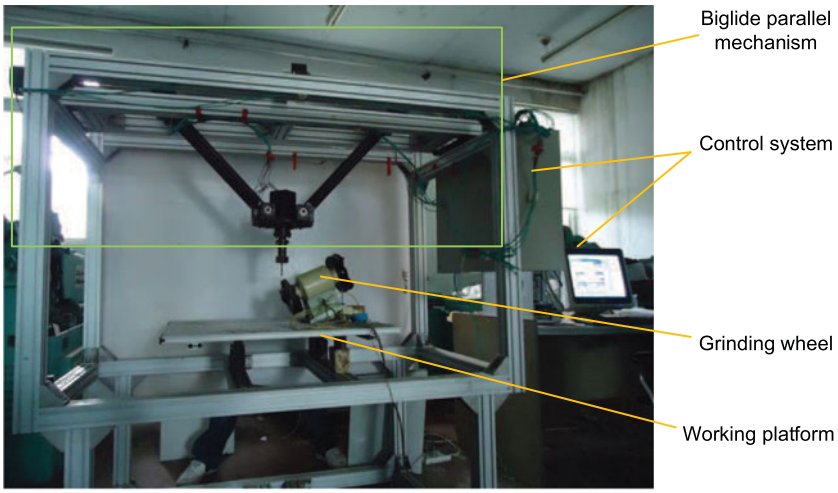


Fig. 1. Prototype of the grinding machine based on the Biglide parallel mechanism.

the coupling between them, where the spring compliance is evaluated based on the concept of the Finite Element Analysis (FEA) approach. Compared to FEA, this approach gives high computation accuracy but with less computational consumption, which will be adopted in this work.

On the assessment of the general 6×6 stiffness matrix, one problem usually encounters is that the matrix is dimensionally inhomogeneous, which does not admit a norm to evaluate the manipulator stiffness. A widely adopted approach to overcome this problem is the eigenscrew decomposition of the stiffness or compliance matrix,[11–14] which is not applicable to evaluate the manipulator stiffness for the overall workspace (WS). Recently, the principal axis decomposition through congruence transformation was proposed by making use of the eigenvectors of the translational entry in the stiffness matrix.[15] Kövecses and Ebrahimi[16] proposed a decomposition of the dynamic inertia matrix by transforming variables into dimensionless parameters, which can be applied to the stiffness matrix.[17] In the work of Angeles,[18] it is proved that a Cartesian stiffness matrix can be decoupled if and only if its coupling entry is singular. The decoupling of the stiffness matrix leads to two separate stiffness matrices, allowing the evaluation of the translational and rotational stiffnesses, respectively, which is applicable to the parallel Biglide grinder.

In this paper, the stiffness of the grinding machine based on the parallel Biglide mechanism in Fig. 1 with two alternative modular parallelograms, as shown in Fig. 2, which is used for twist drill grinding, was investigated for comparison. The stiffness matrices of the two spatial modules, respectively, were derived and discussed. The stiffness characteristics of the two Biglide machines were analyzed and compared by the decoupling of the Cartesian stiffness matrix, through which the principal stiffnesses and their directions were identified.

2. Manipulator Architecture

Figure 2(a) and 2(b) illustrate the serial-parallel Biglide parallel mechanism,[19] which has a decoupled translation along the normal to the plane of parallel mechanism's motion. The part of parallel mechanism, a two degree-of-freedom (2-dof) planar PM, can generate two translations in the horizontal/vertical directions, consisting of two modular parallelograms connected to the mobile platform (MP) and two sliding units, where the sliding unit is actuated via lead screw system. Moreover, with an additional actuator attached to the MP, its end-effector can generate a rotation around the vertical axis. Thus, this hybrid mechanism can produce either 3-dof pure translations or SCARA (Selective Compliance Assembly Robot Arm) motion. It is noted that the parallelogram can be replaced with an alternative structure,[20] and Fig. 2(c) displays another alternative structure, of which four gimbal axes (one gimbal axis from one universal joint) are parallel.

The kinematic structures of the two alternative machines are depicted in Fig. 3. A reference coordinate frame $(x,\ y,\ z)$ is built on the top of the mounting frame, with the origin O located at the geometric center. The x-axis is parallel to segment A_1A_2 and z-axis is parallel to the vertical axis

https://doi.org/10.1017/S0263574716000059 Published online by Cambridge University Press

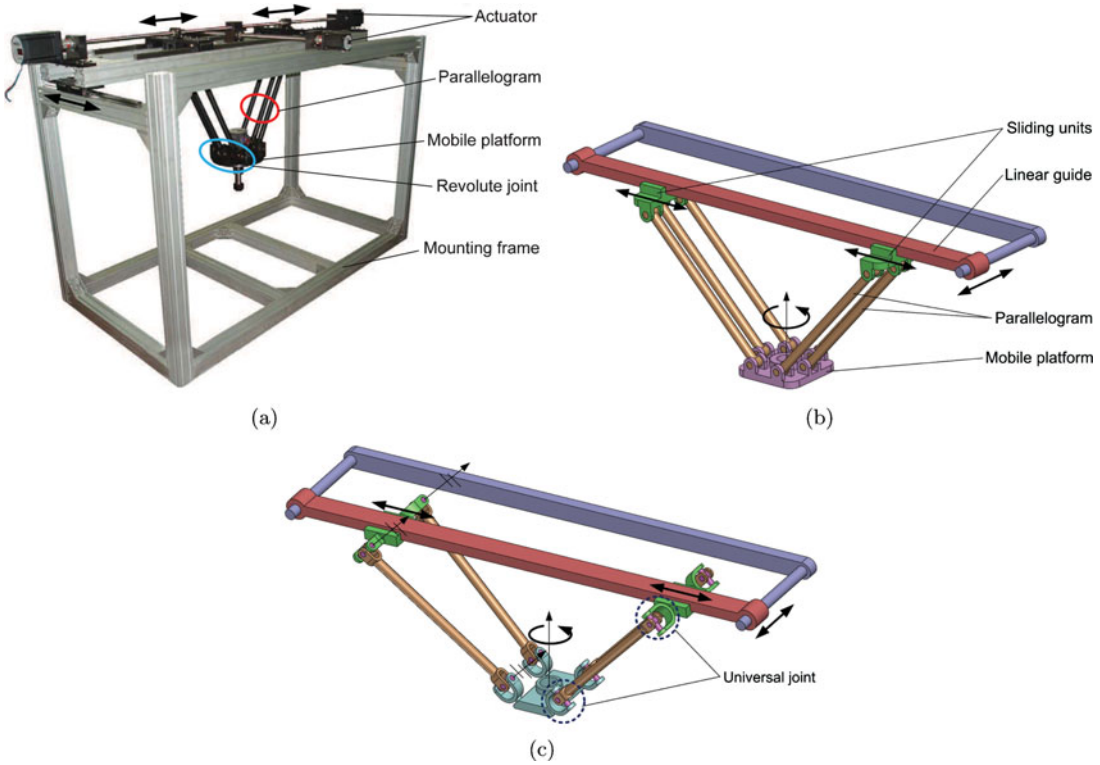


Fig. 2. The Biglide parallel grinder: (a) the prototype; (b) the simplified CAD model of the original mechanism; (c) the alternative CAD model.

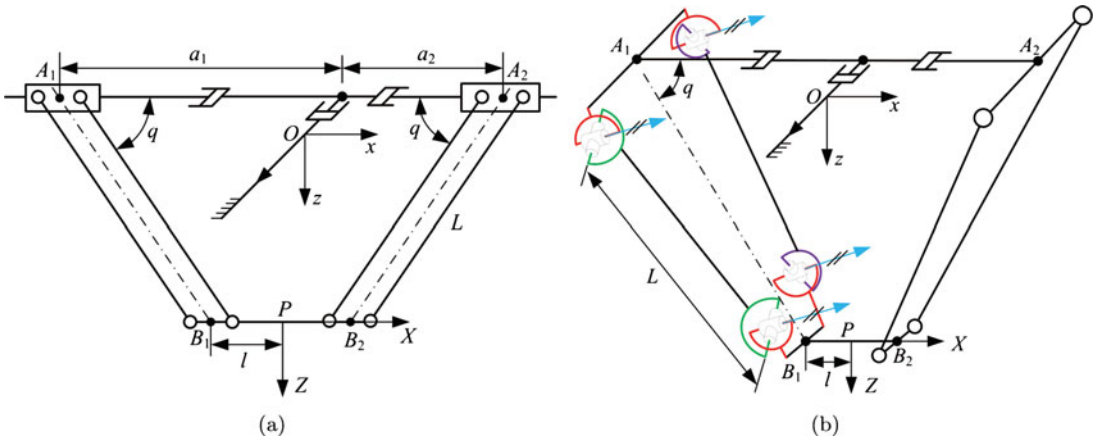


Fig. 3. The kinematic structure of the Biglide parallel machine: (a) original; (b) alternative.

pointing downwards. A moving frame $(X,\ Y,\ Z)$ is attached to the MP, with the origin P located at the geometric center, of which the coordinate axes are parallel to those of the reference frame. The x-coordinate of point A_i in the frame $(x,\ y,\ z)$ is denoted by a_i.

3. Mobility Analysis of the Alternative Biglide Manipulator

The degree-of-freedom of the alternative parallel Biglide mechanism is derived by the Group Theory. As shown in Fig. 4, the kinematic bond $\mathcal{L}_{ij}$ of the ijth linkage, $i,\ j \in \{1,\ 2\}$, is the product of the following four bonds:

- The translation subgroup $\mathcal{T}(\chi)$ passing through A_i and parallel to x-axis.
- The rotation subgroup $\mathcal{R}(\mathcal{A}_i)$ passing through A_{ij} and parallel to $\mathcal{A}_i$.

https://doi.org/10.1017/S0263574716000059 Published online by Cambridge University Press

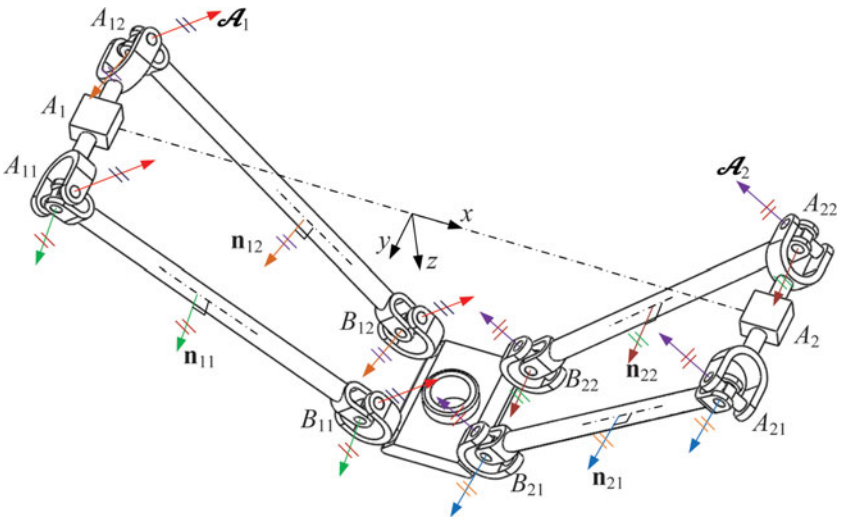


Fig. 4. The alternative parallel Biglide manipulator with linear inputs.

- The translation subgroup $\mathcal{T}(\mathbf{n}_{ij})$ lying in a plane ε_{ij} normal to $\mathbf{n}_{ij}$.
- The rotation subgroup $\mathcal{R}(\mathcal{A}_i)$ passing through B_{ij} and parallel to $\mathcal{A}_i$.

Thus, the kinematic bonds $\mathcal{L}_{ij}$ of the ijth chain is

$$\mathcal{L}_{ij} = \mathcal{T}(\chi) \cdot \mathcal{R}(\mathcal{A}_i) \cdot \mathcal{T}(\mathbf{n}_{ij}) \cdot \mathcal{R}(\mathcal{A}_i). \tag{1}$$

Subsequently, the kinematic bonds $\mathcal{L}_i$ of the ith limb is

$$\mathcal{L}_i = \mathcal{L}_{i1} \cap \mathcal{L}_{i2} = \mathcal{T}(\chi) \cdot \mathcal{R}(\mathcal{A}_i) \cdot \mathcal{T}(\mathbf{n}_i), \tag{2}$$

where $\mathcal{T}(\mathbf{n}_i)$ is a translation subgroup parallel to $\mathbf{n}_i$, $\mathbf{n}_i$ being the common unit vector lies in the planes ε_{i1} and ε_{i2}. Equation (2) has the equivalent expression $\mathcal{L}_i = \mathcal{Y}(y) \cdot \mathcal{R}(\mathcal{A}_i)$, where $\mathcal{Y}(y)$ is the planar translation subgroup normal to the y-axis. Therefore, the intersection of the two limbs yields

$$\mathcal{L} = \mathcal{L}_1 \cap \mathcal{L}_2 = \mathcal{Y}(y). \tag{3}$$

Henceforth, the intersection of all subgroups being a planar translation subgroup normal to the y-axis, the robot generates the 2-dof translation.

4. Stiffness Modeling of the Biglide Grinder

The manipulator stiffness is configuration-dependent and related to the stiffness of the actuators and links. In order to evaluate the influence of the geometric parameters of the manipulator architecture and the link dimensions as well as the end-effector position/orientation to the manipulator stiffness, an analytical stiffness modeling approach is essential to calculate the stiffness matrix of the manipulator, in which the analytical model can be readily used for manipulator parameterization and design optimization.[21]

In this work, the stiffness model is established with the virtual-spring approach[9] based on the screw coordinates,[22] as this approach considers the actuator/link deflections and the influence of the passive joints simultaneously to provide high computation accuracy as the FEA approach with less time consumption. The following assumptions are made: (1) unloaded equilibrium; (2) frictionless joints; (3) rigid base and mobile platforms. With the previous assumptions, the stiffness subject to actuators and limbs are derived as follows:

https://doi.org/10.1017/S0263574716000059 Published online by Cambridge University Press

4.1. Actuation stiffness

The translation of the sliding unit of the machine is realized through the lead screw system, thus, the actuation stiffness is calculated by considering both the actuator stiffness and the lead screw stiffness in its axial direction. For a lead screw actuation system, the torque τ of the actuator can be expressed as ref. [23]

$$\tau = K_{act}\Delta\gamma, \tag{4}$$

where K_{act} and $\Delta\gamma$ denote the torsional stiffness of the actuator and the angular deflection, respectively.

Lead screw transforms the input torque τ to linear force f,[24] namely,

$$f = \frac{2\tau}{d_p \tan(\vartheta + \nu)}, \tag{5}$$

with

$$\vartheta = \tan^{-1}\frac{l_s}{\pi d_p}; \quad \nu = \tan^{-1}\frac{\mu}{\cos\alpha_t}, \tag{6}$$

where d_p and l_s stand for the pitch diameter and the lead of the ball screw, respectively. Moreover, ϑ and ν, respectively, denote the lead angle and friction angle, μ and α_t being the friction coefficient and the radial angle of thread. As a result, the angular deflection is transformed into linear deformation expressed as

$$\Delta a = l_s\Delta\gamma. \tag{7}$$

Combining Eqs. (4), (5) and (7), the actuation stiffness K_a is derived from $f = K_a\Delta a$ with the consideration of the stiffness of the screw shaft, namely,

$$K_a = \left[\frac{d_p l_s \tan(\vartheta + \nu)}{2K_{act}} + \frac{L_s}{EA_s}\right]^{-1}, \tag{8}$$

where L_s and A_s are the length and the cross-section area of the screw shaft, respectively, and E is the Young's modulus.

4.2. Stiffness matrix of parallelogram

The structure of the parallelogram link is shown in Fig. 5, of which the stiffness matrix is calculated with the virtual-spring approach. The elastic deformation $\delta\mathbf{t}_1$ of the free end in the U_1V_1 chain can be expressed as

$$\delta\mathbf{t}_1 = \mathbf{J}_\theta^{\Pi 1}\delta\boldsymbol{\theta}_{\Pi 1} + \mathbf{J}_q^{\Pi 1}\delta\mathbf{q}_{\Pi 1}, \tag{9}$$

where $\mathbf{J}_\theta^{\Pi 1}$ is the Jacobian matrix corresponding to the deflections $\delta\boldsymbol{\theta}_{\Pi 1}$ and $\mathbf{J}_q^{\Pi 1}$ is the Jacobian matrix to consider the influence of the passive joints, expressed as

$$\mathbf{J}_\theta^{\Pi 1} = \begin{bmatrix} 1 & 0 & 0 & 0 & 0 & 0 \\ 0 & 1 & 0 & 0 & 0 & 0 \\ 0 & 0 & 1 & 0 & 0 & 0 \\ 0 & -\frac{h\mathrm{S}_q}{2} & 0 & 1 & 0 & 0 \\ \frac{h\mathrm{S}_q}{2} & 0 & -\frac{h\mathrm{C}_q}{2} & 0 & 1 & 0 \\ 0 & \frac{h\mathrm{C}_q}{2} & 0 & 0 & 0 & 1 \end{bmatrix}; \quad \mathbf{J}_q^{\Pi 1} = \begin{bmatrix} 0 & 0 \\ 1 & 1 \\ 0 & 0 \\ \frac{h\mathrm{S}_q}{2} & \frac{h\mathrm{S}_q}{2} \\ 0 & 0 \\ -\frac{h\mathrm{C}_q}{2} - L & -\frac{h\mathrm{C}_q}{2} \end{bmatrix}, \tag{10}$$

where $\mathrm{S}_q = \sin q$, $\mathrm{C}_q = \cos q$. Let the external wrench (a six-dimensional array of forces and moments) applied to the free end of U_1V_1 chain be $\mathbf{f}_1$, and the force/torque causing the deflection

https://doi.org/10.1017/S0263574716000059 Published online by Cambridge University Press

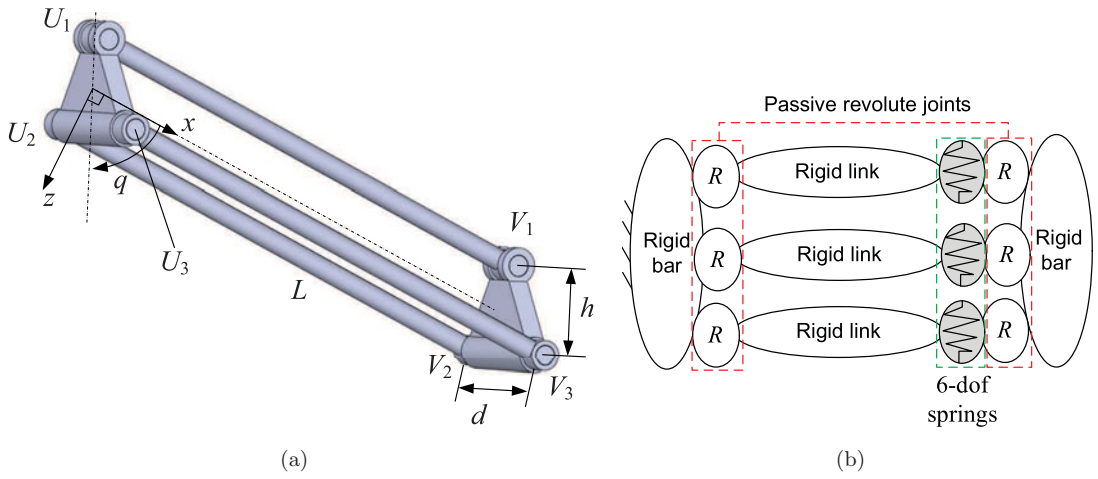


Fig. 5. The parallelogram linkage: (a) coordinate and parameters; (b) virtual-spring model.

being denoted by $\boldsymbol{\tau}_{\Pi 1}$, the equilibrium condition for U_1V_1 chain is written as

$$\boldsymbol{\tau}_1 = \left(\mathbf{J}_\theta^{\Pi 1}\right)^T \mathbf{f}_1, \quad \boldsymbol{\tau}_{\Pi 1} = \mathbf{K}_{\text{bar}} \delta\boldsymbol{\theta}_{\Pi 1}, \quad \left(\mathbf{J}_q^{\Pi 1}\right)^T \mathbf{f}_1 = \mathbf{0}, \tag{11}$$

and $\mathbf{K}_{\text{bar}} = [k_{ij}]$ is the bar-link stiffness matrix, calculated by a cantilever, which takes the following form:

$$\mathbf{K}_{\text{bar}} = \begin{bmatrix} \frac{GI_x}{L} & 0 & 0 & 0 & 0 & 0 \\ 0 & \frac{4EI_y}{L} & 0 & 0 & 0 & \frac{6EI_y}{L^2} \\ 0 & 0 & \frac{4EI_z}{L} & 0 & -\frac{6EI_z}{L^2} & 0 \\ 0 & 0 & 0 & \frac{EA}{L} & 0 & 0 \\ 0 & 0 & -\frac{6EI_z}{L^2} & 0 & \frac{12EI_z}{L^3} & 0 \\ 0 & \frac{6EI_y}{L^2} & 0 & 0 & 0 & \frac{12EI_y}{L^3} \end{bmatrix}, \tag{12}$$

where L is the link length, A is its cross-section area, I_y, I_z and I_x are the quadratic and polar moments of inertia of the cross-section, and E and G are the Young's and shear modules, respectively.

Combining Eqs. (9) and (11), the kinetostatic model of U_1V_1 chain is reduced to

$$\begin{bmatrix} \mathbf{J}_\theta^{\Pi 1} \mathbf{K}_{\text{bar}}^{-1} \left(\mathbf{J}_\theta^{\Pi 1}\right)^T & \mathbf{J}_q^{\Pi 1} \\ \left(\mathbf{J}_q^{\Pi 1}\right)^T & \mathbf{0}_2 \end{bmatrix} \begin{bmatrix} \mathbf{f}_1 \\ \delta\mathbf{q}_{\Pi 1} \end{bmatrix} = \begin{bmatrix} \delta\mathbf{t}_1 \\ \mathbf{0} \end{bmatrix}. \tag{13}$$

The stiffness matrix $\mathbf{K}_{\Pi,1}$ of U_1V_1 chain in the parallelogram is the first six-dimensional entry extracted for the matrix below:[9]

$$\mathbf{K}'_{\Pi,1} = \begin{bmatrix} \mathbf{J}_\theta^{\Pi 1} \mathbf{K}_{\text{bar}}^{-1} \left(\mathbf{J}_\theta^{\Pi 1}\right)^T & \mathbf{J}_q^{\Pi 1} \\ \left(\mathbf{J}_q^{\Pi 1}\right)^T & \mathbf{0}_2 \end{bmatrix}^{-1}. \tag{14}$$

Similarly, the stiffness matrices $\mathbf{K}_{\Pi,2}$ and $\mathbf{K}_{\Pi,3}$ of the chains U_2V_2 and U_3V_3 can be readily found. After the elimination of the zero column and row, the stiffness matrix of parallelogram link is

https://doi.org/10.1017/S0263574716000059 Published online by Cambridge University Press

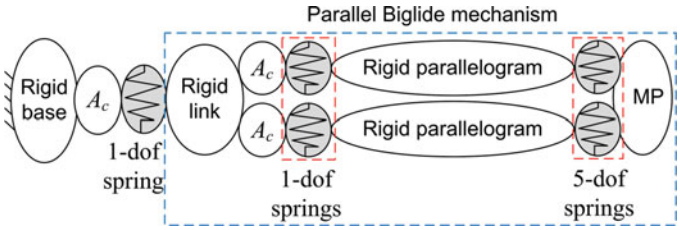


Fig. 6. The virtual-spring model of the serial-parallel Biglide manipulator.

calculated by a simple addition $\mathbf{K}_\Pi = \Sigma_{i=1}^{3}\mathbf{K}_{\Pi,i}$, namely,

$$\mathbf{K}_\Pi = 3\cdot\left[\begin{array}{ccc|cc} k_{11}+\frac{k_{55}h^2\mathrm{S}_q^2}{4} & 0 & -\frac{k_{35}h\mathrm{S}_q}{6}-\frac{k_{55}h^2\mathrm{S}_q}{8} & 0 & -\frac{k_{55}h\mathrm{S}_q}{2} \\ 0 & \frac{k_{44}h^2\mathrm{S}_q^2}{4} & 0 & \frac{k_{44}h\mathrm{S}_q}{2} & 0 \\ -\frac{k_{35}h\mathrm{S}_q}{6}-\frac{k_{55}h^2\mathrm{S}_q}{8} & & k_{33}+\frac{k_{44}d^2}{6}+\frac{k_{35}h\mathrm{C}_q}{3}+\frac{k_{55}h^2\mathrm{C}_q^2}{4} & 0 & k_{35}+\frac{k_{55}h\mathrm{C}_q}{6} \\ \hline & \frac{k_{44}h\mathrm{S}_q}{2} & 0 & k_{44} & 0 \\ -\frac{k_{55}h\mathrm{S}_q}{2} & 0 & k_{35}+\frac{k_{55}h\mathrm{C}_q}{6} & 0 & k_{55} \end{array}\right], \quad (15)$$

where k_{ij} stand for the non-zero elements in matrix (12). It appears that the translational stiffness in z-axis degenerates to zero due to the passive joints. The rotational stiffness about y-axis is described by the axial stiffness k_{44} of a beam and will reduce to zero in the singular configuration of $q = 0$, namely, the three beams being coplanar. On the other hand, the rotational stiffness about z-axis achieves its maximum value with $q = 0$. Moreover, when $q = \pi/2$, both the rotational stiffnesses about x- and y-axis reach up to their peak values, but the rotational stiffness about z-axis becomes the smallest in its range.

4.3. Cartesian stiffness matrix of the manipulator

The manipulator in the study has a serial-parallel structure, as displayed in Fig. 6, of which the Cartesian stiffness matrix $\mathbf{K}$ of the parallel Biglide mechanism is firstly computed with the virtual-spring approach. In accordance with Fig. 6, the equilibrium condition of the limb A_1B_1 in Fig. 2(b) is derived as

$$\$_{P1} = \mathbf{J}_{\theta 1}\delta\boldsymbol{\theta}_1, \quad \boldsymbol{\tau}_1 = \mathbf{J}_{\theta 1}^T\mathbf{w}_1, \quad \boldsymbol{\tau}_1 = \mathbf{K}_\theta\delta\boldsymbol{\theta}_1, \quad (16)$$

where $\$_{P1}$ is the small-amplitude deformation screw and $\mathbf{w}_1$ is the external wrench exerted on the MP. On the other hand, $\delta\boldsymbol{\theta}_1$ is a vector of the deflections caused by the forces/moments $\boldsymbol{\tau}_1$ in the joint space. Moreover, $\mathbf{J}_{\theta 1}$ and $\mathbf{K}_\theta$, respectively, are the Jacobian matrix related to the deflections and the stiffness matrix in the joint space, expressed as

$$\mathbf{J}_{\theta 1} = \begin{bmatrix} 0 & \mathrm{C}_q & 0 & -\mathrm{S}_q & 0 & 0 \\ 0 & 0 & 1 & 0 & 0 & 0 \\ 0 & \mathrm{S}_q & 0 & \mathrm{C}_q & 0 & 0 \\ 1 & 0 & 0 & 0 & \mathrm{C}_q & 0 \\ 0 & r\mathrm{S}_q & 0 & r\mathrm{C}_q & 0 & 1 \\ 0 & 0 & -r & 0 & \mathrm{S}_q & 0 \end{bmatrix}; \quad \mathbf{K}_\theta = \begin{bmatrix} K_a\mathrm{C}_q & 0 \\ 0 & \mathbf{K}_\Pi \end{bmatrix}. \quad (17)$$

Consequently, the Cartesian stiffness matrix of limb A_1B_1 is found as $\mathbf{K}_1 = \mathbf{J}_{\theta 1}^{-T}\mathbf{K}_\theta\mathbf{J}_{\theta 1}^{-1}$. For limb A_2B_2, the expressions are similar, wherein the Jacobian matrix can be obtained by replacing q with $\pi - q$ and changing the signs of r.

From $\$_P = \$_{Pi}$, $\mathbf{w} = \Sigma_{i=1}^{2}\mathbf{w}_i$, $\mathbf{w}_i = \mathbf{K}_i\$_{Pi}$, $i = 1, 2$, the Cartesian stiffness matrix of the parallel Biglide mechanism is the summation of the stiffness matrices of the two limbs, namely, $\mathbf{K} = \mathbf{K}_1 + \mathbf{K}_2$.

https://doi.org/10.1017/S0263574716000059 Published online by Cambridge University Press

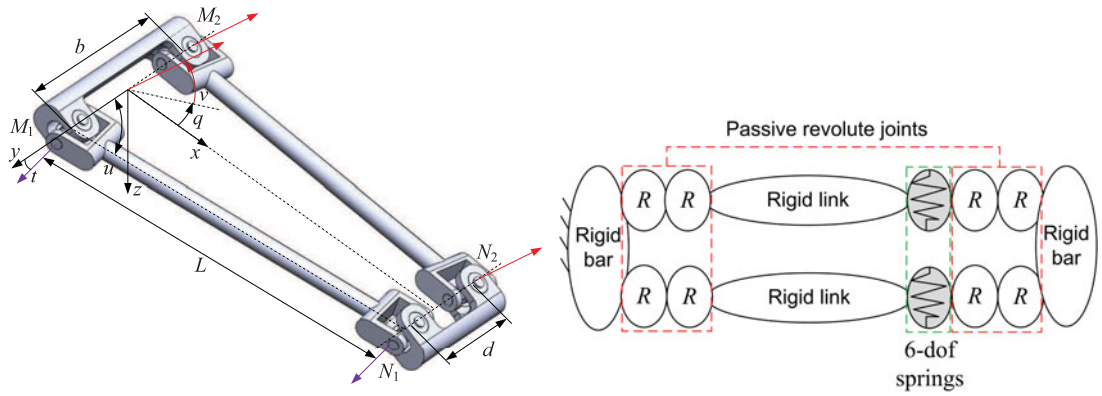


Fig. 7. The structure of the alternative parallelogram: (a) coordinate and parameters; (b) virtual-spring model.

To this end, the Cartesian stiffness matrix of the Biglide manipulator is calculated below

$$\mathbf{K} = \begin{bmatrix} \mathbf{K}_{rr} & \mathbf{K}_{rt} \\ \mathbf{K}_{rt}^T & \mathbf{K}_{tt} \end{bmatrix} = \left[\begin{array}{ccc|ccc} K_{11} & 0 & K_{13} & 0 & K_{15} & 0 \\ 0 & K_{22} & 0 & K_{24} & 0 & K_{26} \\ K_{13} & 0 & K_{33} & 0 & K_{35} & 0 \\ \hline 0 & K_{24} & 0 & K_{44} & 0 & 0 \\ K_{15} & 0 & K_{35} & 0 & K_{55} & 0 \\ 0 & K_{26} & 0 & 0 & 0 & K_{66} \end{array}\right], \tag{18}$$

where the non-zero elements are given in Appendix A. When $q = \pi/2$, there is no translational stiffness in x-direction, and as a result, the rank of the stiffness matrix decreases to 5, corresponding to the parallel singularity. When $q = 0$, both the serial and parallel singularities occur, which leads to the vanished rotational stiffness about y-direction and translational stiffness in z-direction. Moreover, the translational stiffness K_{55} depends on the bending stiffness of the bar link independent of the manipulator configuration.

With the consideration of the decoupled translation, the Cartesian stiffness matrix of the serial-parallel manipulator, which has the similar form as matrix (18), can be rewritten as

$$\mathbf{K}_c = \left(\mathbf{K}^{-1} + K_a^{-1}\mathbf{s}\mathbf{s}^T\right)^{-1}; \quad \mathbf{s} = \begin{bmatrix} 0 & 0 & 0 & 0 & 1 & 0 \end{bmatrix}^T. \tag{19}$$

4.4. Stiffness of the grinder with alternative parallelograms

Referring to Sections 4.2 and 4.3, the stiffness matrix of the manipulator with the alternative parallelograms as displayed in Fig. 2(c) can also be derived, where the difference lies in stiffness matrix of the spatial modular parallelograms. Figure 7 shows the alternative parallelogram, for which the Jacobian matrices corresponding to the deflections and the displacements of the passive joints in the chain M_1N_1 are found as

$$\mathbf{J}_\theta^{b1} = \begin{bmatrix} \mathrm{S}_u & \mathrm{C}_u & 0 & 0 & 0 & 0 \\ -\mathrm{C}_u & \mathrm{S}_u & 0 & 0 & 0 & 0 \\ 0 & 0 & 1 & 0 & 0 & 0 \\ 0 & 0 & \frac{d}{2} & \mathrm{S}_u & \mathrm{C}_u & 0 \\ 0 & 0 & 0 & -\mathrm{C}_u & \mathrm{S}_u & 0 \\ -\frac{d\mathrm{S}_u}{2} & -\frac{d\mathrm{C}_u}{2} & 0 & 0 & 0 & 1 \end{bmatrix}; \quad \mathbf{J}_q^{b1} = \begin{bmatrix} \mathrm{C}_{qv} & \mathrm{S}_{qv}\mathrm{S}_t & \mathrm{C}_{qv} & \mathrm{S}_{qv}\mathrm{S}_t \\ 0 & \mathrm{C}_t & 0 & \mathrm{C}_t \\ -\mathrm{S}_{qv} & \mathrm{C}_{qv}\mathrm{S}_t & -\mathrm{S}_{qv} & \mathrm{C}_{qv}\mathrm{S}_t \\ -\frac{b\mathrm{S}_{qv}}{2} & \frac{b\mathrm{C}_{qv}\mathrm{S}_t}{2} & -\frac{d\mathrm{S}_{qv}}{2} & \frac{d\mathrm{C}_{qv}\mathrm{S}_t}{2} \\ -L\mathrm{S}_{qv} & L\mathrm{C}_{qv}\mathrm{S}_t & 0 & 0 \\ -\frac{b\mathrm{C}_{qv}}{2} & -L\mathrm{C}_t - \frac{b\mathrm{S}_{qv}\mathrm{S}_t}{2} & -\frac{d\mathrm{C}_{qv}}{2} & -\frac{d\mathrm{S}_{qv}\mathrm{S}_t}{2} \end{bmatrix}, \tag{20}$$

https://doi.org/10.1017/S0263574716000059 Published online by Cambridge University Press

where $\mathrm{C}_{qv} = \cos(q + v)$, $\mathrm{S}_{qv} = \sin(q + v)$, and the angle t is solved according to the geometric relationship of the module as below

$$t = -2\tan^{-1}\frac{\mathrm{S}_u\mathrm{S}_v - \sqrt{\mathrm{C}_u^2 + \mathrm{S}_u^2\mathrm{S}_v^2}}{\mathrm{C}_u}. \tag{21}$$

Likewise, the stiffness matrix $\mathbf{K}_P$ of the alternative parallelogram, similar to Eq. (14), is a simple addition of the stiffness matrices of the two linkages. It should be noted that the rank of $\mathbf{K}_P$ is equal to 4 while its size is 5×5, whereas, it is still available to compute the stiffness matrix of the manipulator, by replacing $\mathbf{K}_\Pi$ with $\mathbf{K}_P$ in Eq. (17). Compared to matrix (19), the elements K_{13}, K_{26} and K_{35} in the Cartesian stiffness matrix $\mathbf{K}_c'$ of the alternative Biglide grinder degrade to null.

5. Decoupling of the Stiffness Matrix

Decoupling of the Cartesian stiffness matrix is possible if and only if the 3×3 off-diagonal entry is singular,[18] which is achieved by means of a similarity transformation that involves only a shift of the origin. In view of Eq. (19), the entry $\mathbf{K}_{rt}$ is singular, namely, $\mathrm{rank}(\mathbf{K}_{rt}) \leq 2$, which means that the Cartesian stiffness matrix of the Biglide grinder can be decoupled.

Let the stiffness matrix under study be denoted by $[\mathbf{K}]_\mathcal{A}$ when represented in a coordinate frame labeled by $\mathcal{A}$. Similarly, $[\mathbf{K}]_\mathcal{B}$ stands for the same matrix in a second frame $\mathcal{B}$, under the assumption that the orientation of the axes and origins of the two frames are different. The matrices $[\mathbf{K}]_\mathcal{A}$ and $[\mathbf{K}]_\mathcal{B}$ are displayed below

$$[\mathbf{K}]_\mathcal{A} = \begin{bmatrix} \mathbf{K}_{rr} & \mathbf{K}_{rt} \\ \mathbf{K}_{rt}^T & \mathbf{K}_{tt} \end{bmatrix}; \quad [\mathbf{K}]_\mathcal{B} = \begin{bmatrix} \mathbf{K}_{rr}' & \mathbf{K}_{rt}' \\ \mathbf{K}_{rt}'^T & \mathbf{K}_{tt}' \end{bmatrix}. \tag{22}$$

Thus, the coordinate transformation that relates $[\mathbf{K}]_\mathcal{A}$ with $[\mathbf{K}]_\mathcal{B}$ between different reference frames $\mathcal{A}$ and $\mathcal{B}$[25] can be derived readily as

$$[\mathbf{K}]_\mathcal{B} = \mathbf{\Gamma S \Gamma}^{-1}[\mathbf{K}]_\mathcal{A}\mathbf{S}^{-1}, \tag{23}$$

with the 6×6 permutation matrix $\mathbf{\Gamma}$ defined in its block form as below

$$\mathbf{\Gamma} = \begin{bmatrix} \mathbf{0}_3 & \mathbf{1}_3 \\ \mathbf{1}_3 & \mathbf{0}_3 \end{bmatrix} \tag{24}$$

and

$$\mathbf{S} = \begin{bmatrix} \mathbf{Q} & \mathbf{0}_3 \\ \mathbf{DQ} & \mathbf{Q} \end{bmatrix}; \quad \mathbf{\Gamma S \Gamma}^{-1} = \mathbf{\Gamma S \Gamma} = \begin{bmatrix} \mathbf{Q} & \mathbf{DQ} \\ \mathbf{0}_3 & \mathbf{Q} \end{bmatrix}, \tag{25}$$

where $\mathbf{Q}$ denotes the rotation matrix from the frame $\mathcal{B}$ to $\mathcal{A}$, while $\mathbf{D}$ is the cross-product matrix (CPM) of the displacement $\mathbf{d}$ that carries the origin of frame $\mathcal{B}$ into that of $\mathcal{A}$, defined as $\mathbf{D} = \mathrm{CPM}(\mathbf{d})$.[26]

The expanded form of the congruence transformation (23) of spatial stiffness can be given by

$$\mathbf{K}_{rr}' = \mathbf{Q}(\mathbf{K}_{rr} - \mathbf{K}_{rt}\mathbf{D})\mathbf{Q}^T + \mathbf{DQ}(\mathbf{K}_{rt}^T - \mathbf{K}_{tt}\mathbf{D})\mathbf{Q}^T \tag{26a}$$

$$\mathbf{K}_{rt}' = (\mathbf{QK}_{rt} + \mathbf{DQK}_{tt})\mathbf{Q}^T \tag{26b}$$

$$\mathbf{K}_{tt}' = \mathbf{QK}_{tt}\mathbf{Q}^T. \tag{26c}$$

https://doi.org/10.1017/S0263574716000059 Published online by Cambridge University Press

Table I. The geometric parameters and properties of the Biglide parallel grinder.

Original Biglide machine				Alternative			Bar link		
L (mm)	l (mm)	d (mm)	h (mm)	L (mm)	b (mm)	v (deg)	r (mm)	E (GPa)	G (GPa)
500	65	140	35	503	250	45	12.5	211	81

Table II. The parameters of the lead screw system.

K_{act} (Nm/rad)	d_p (mm)	l_s (mm)	μ	α_t (deg)	L_s (mm)	A_s (m^2)	E (GPa)
10^3	16	20	0.01	15	550	$2.01 \cdot 10^{-4}$	211

Under the decoupling condition $\mathbf{K}'_{rt} = \mathbf{0}$, matrix $\mathbf{Q}$ can be freely chosen as the identity matrix $\mathbf{1}$, which yields

$$\mathbf{K}'_{rr} = \mathbf{K}_{rr} - \mathbf{K}_{rt}\mathbf{D} + \mathbf{D}(\mathbf{K}_{rt}^T - \mathbf{K}_{tt}\mathbf{D}) \tag{27a}$$

$$\mathbf{D}\mathbf{K}_{tt} = -\mathbf{K}_{rt} \tag{27b}$$

$$\mathbf{K}'_{tt} = \mathbf{K}_{tt}, \tag{27c}$$

whence $\mathbf{D}$, a 3×3 skew-symmetric matrix, can be determined from Eq. (27b), hence, $\text{rank}(\mathbf{D}\mathbf{K}_{tt}) \leq 2$, in accordance with Sylvester's theorem.[27] Under the assumption that $\mathbf{K}_{rt}$ is singular, $\mathbf{D}$ is found upon taking the axial vector[26] of both sides of Eq. (27b), namely,

$$\mathbf{M}\mathbf{d} = \text{vect}(\mathbf{K}_{rt}); \quad \mathbf{M} = \frac{1}{2}[\mathbf{1}\text{tr}(\mathbf{K}_{tt}) - \mathbf{K}_{tt}], \tag{28}$$

where $\mathbf{M}$ carries unit N/m and $\text{tr}(\mathbf{K}_{tt})$ is the trace of $\mathbf{K}_{tt}$. Operation $\text{vect}(\cdot)$ is the mapping from skew-symmetric matrix to its corresponding vector. If $\mathbf{M}$ is invertible, then $\mathbf{d} = \mathbf{M}^{-1}\text{vect}(\mathbf{K}_{rt})$; otherwise, $\mathbf{M}$ fails to be invertible, but $\mathbf{d}$ can still be calculated.[18]

Upon the decoupled translational and rotational stiffness matrices, the max-/minimum translational and rotational stiffnesses can be identified by virtue of the eigenvalue problem, where the eigenvalues and eigenvectors are considered to represent the principal stiffnesses and directions. The minimum eigenvalues of the translational and rotational stiffness matrices are then defined as the translational and rotational stiffness performance indices, respectively, which can be used in either performance evaluation or optimum design. The larger the indices, the higher rigidity the manipulator. As the stiffness analysis plays a significant role in the manipulator design, the decoupling of stiffness matrix can be applied in this process, through which parameters and dimensions are evaluated to optimize the manipulator performance.

6. Stiffness Performance of the Biglide Machine

In this section, the decoupling of the Cartesian stiffness matrix is applied to the two alternative Biglide machines in Fig. 2, aiming to find the translational and rotational stiffnesses as well as the corresponding directions to characterize the stiffness properties. The geometric parameters are given in Table I together with the bar-link properties, where the link length L of the alternative structure is to guarantee the same WS size as the original mechanism and r is the radius of the circular cross-section of the bar link. Moreover, the parameters of the lead screw system are listed in Table II.

The reachable WS of the parallel Biglide manipulator in the xz plane, subject to the motion ranges of the sliding units of $a_1 \in [-550, -200]$ and $a_2 \in [200, 550]$, is visualized by means of the graphical method, namely, the solid blue area in Fig. 8. Within the reachable WS, the corresponding maximum regular workspace (RWS), i.e., the square region enveloped by the yellow lines in Fig. 8, is found, where the technique introduced by Briot *et al.*[28] is adopted. Due to the symmetrical structure, the manipulator stiffness is independent of x coordinate but depends on z coordinate, therefore, two

https://doi.org/10.1017/S0263574716000059 Published online by Cambridge University Press

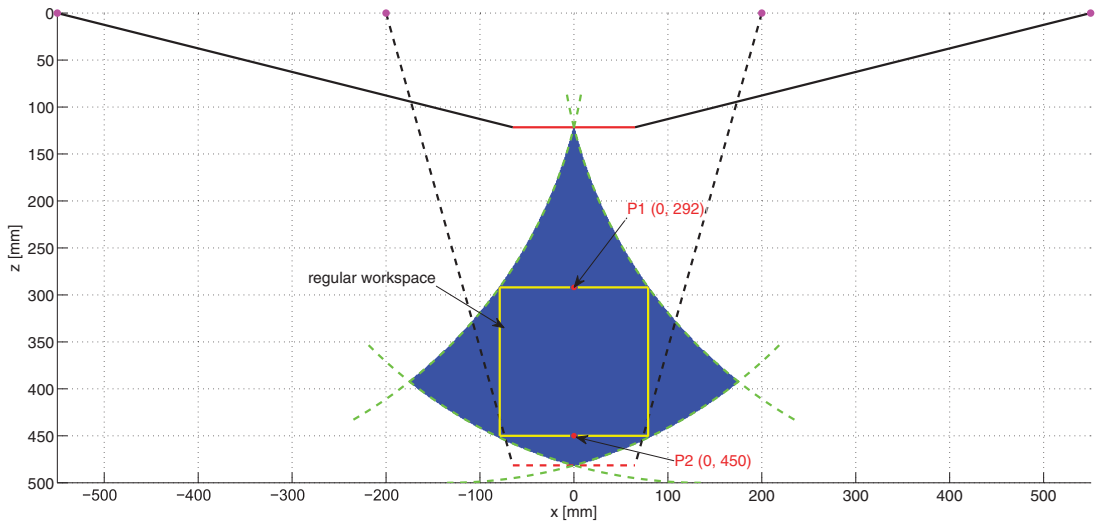


Fig. 8. The reachable and regular workspace of the Biglide parallel grinder.

extreme positions on the RWS upper and lower boundaries, labeled by $P1$ and $P2$, are selected as the representative WS points.

At position $P1$, the Cartesian stiffness matrix of the original Biglide machine is computed as

$$\mathbf{K}_c = \begin{bmatrix} \mathbf{K}_{rr} & \mathbf{K}_{rt} \\ \mathbf{K}_{rt}^T & \mathbf{K}_{tt} \end{bmatrix} = \begin{bmatrix} 1.467 & 0 & 0.001 & 0 & 0.282 & 0 \\ 0 & 15.695 & 0 & -1.867 & 0 & 7.250 \\ 0.001 & 0 & 2.883 & 0 & -0.004 & 0 \\ 0 & -1.867 & 0 & 20.668 & 0 & 0 \\ 0.282 & 0 & -0.004 & 0 & 1.970 & 0 \\ 0 & 7.250 & 0 & 0 & 0 & 3684.179 \end{bmatrix} \cdot 10^6, \tag{29}$$

where the entries $\mathbf{K}_{rr}$, $\mathbf{K}_{rt}$ and $\mathbf{K}_{tt}$ are given in Nm, N and N/m, respectively.

In the decoupling of the stiffness matrix (29), matrix $\mathbf{M}$ in Eq. (28) is computed as

$$\mathbf{M} = \begin{bmatrix} 1.843 & 0 & 0 \\ 0 & 1.852 & 0 \\ 0 & 0 & 0.011 \end{bmatrix} \cdot 10^9 \text{ N/m}, \tag{30}$$

which is invertible, consequently, $\mathbf{d}$ follows the simple inversion of $\mathbf{M}$:

$$\mathbf{d} = \begin{bmatrix} -0.002 & 0 & -0.095 \end{bmatrix}^T \text{ m}. \tag{31}$$

Following the relation $\mathbf{D} = \text{CPM}(\mathbf{d})$, one obtains:

$$\mathbf{D} = \begin{bmatrix} 0 & 0.095 & 0 \\ -0.095 & 0 & 0.002 \\ 0 & -0.002 & 0 \end{bmatrix} \text{ m}. \tag{32}$$

Substituting matrix $\mathbf{D}$ into Eqs. (27a) and (27c), $\mathbf{K}'_{rr}$ and $\mathbf{K}'_{tt}$ are calculated as

$$\mathbf{K}'_{rr} = \begin{bmatrix} 0.154 & 0 & 0 \\ 0 & 1.628 & 0 \\ 0 & 0 & 0.288 \end{bmatrix} \cdot 10^7 \text{ Nm}; \quad \mathbf{K}'_{tt} = \begin{bmatrix} 0.021 & 0 & 0 \\ 0 & 0.002 & 0 \\ 0 & 0 & 3.684 \end{bmatrix} \cdot 10^9 \text{ N/m}. \tag{33}$$

Matrix $\mathbf{K}_c$ is decoupled into two homogeneous sub-matrices corresponding to the translational and rotational stiffnesses, thus, resorting to the eigenvalue problem, one can identify the directions along

https://doi.org/10.1017/S0263574716000059 Published online by Cambridge University Press

which the max-/minimum principal stiffness exist. The corresponding eigenvalues and eigenvectors of $\mathbf{K}'_{rr}$ ($\mathbf{K}'_{tt}$), stored in arrays $\boldsymbol{\lambda}_{rr}$ ($\boldsymbol{\lambda}_{tt}$) and matrices $\boldsymbol{\Lambda}_{rr}$ ($\boldsymbol{\Lambda}_{tt}$), respectively, are displayed below

$$\boldsymbol{\lambda}_{rr} = \begin{bmatrix} 0.154 \\ 1.628 \\ 0.288 \end{bmatrix} \cdot 10^7\,\text{Nm},\ \boldsymbol{\Lambda}_{rr} = \begin{bmatrix} 1 & 0 & 0 \\ 0 & 1 & 0 \\ 0 & 0 & 1 \end{bmatrix};\quad \boldsymbol{\lambda}_{tt} = \begin{bmatrix} 0.021 \\ 0.002 \\ 3.684 \end{bmatrix} \cdot 10^9\,\text{N/m},\ \boldsymbol{\Lambda}_{tt} = \begin{bmatrix} 1 & 0 & 0 \\ 0 & 1 & 0 \\ 0 & 0 & 1 \end{bmatrix}. \tag{34}$$

At the same position $P1$, the Cartesian stiffness matrix $\mathbf{K}'_c$ of the alternative Biglide machine in Fig. 2(c) is found as

$$\mathbf{K}'_c = \begin{bmatrix} 0.779 & 0 & 0 & 0 & -2.063 & 0 \\ 0 & 10.250 & 0 & -1.867 & 0 & 0 \\ 0 & 0 & 2.020 & 0 & 0 & 0 \\ 0 & -1.867 & 0 & 20.668 & 0 & 0 \\ -2.063 & 0 & 0 & 0 & 5.552 & 0 \\ 0 & 0 & 0 & 0 & 0 & 2425.992 \end{bmatrix} \cdot 10^6. \tag{35}$$

Solving the eigenvalue problem of the decoupled translational and rotational stiffness matrices, the eigenvalues $\boldsymbol{\lambda}'_{rr}$ ($\boldsymbol{\lambda}'_{tt}$) and eigenvectors $\boldsymbol{\Lambda}'_{rr}$ ($\boldsymbol{\Lambda}'_{tt}$) are obtained below

$$\boldsymbol{\lambda}'_{rr} = \begin{bmatrix} 0.081 \\ 1.022 \\ 0.202 \end{bmatrix} \cdot 10^7\,\text{Nm},\ \boldsymbol{\Lambda}'_{rr} = \begin{bmatrix} 1 & 0 & 0 \\ 0 & 1 & 0 \\ 0 & 0 & 1 \end{bmatrix};\quad \boldsymbol{\lambda}'_{tt} = \begin{bmatrix} 0.021 \\ 0.006 \\ 2.426 \end{bmatrix} \cdot 10^9\,\text{N/m},\ \boldsymbol{\Lambda}'_{tt} = \begin{bmatrix} 1 & 0 & 0 \\ 0 & 1 & 0 \\ 0 & 0 & 1 \end{bmatrix}. \tag{36}$$

Similarly, the six eigenvalues at position $P2$ of the two alternative manipulators, respectively, are calculated as

$$\boldsymbol{\lambda}_{rr} = \begin{bmatrix} 3.493 \\ 6.987 \\ 0.881 \end{bmatrix} \cdot 10^6,\ \boldsymbol{\lambda}_{tt} = \begin{bmatrix} 0.011 \\ 0.002 \\ 1.537 \end{bmatrix} \cdot 10^9;\quad \boldsymbol{\lambda}'_{rr} = \begin{bmatrix} 3.075 \\ 4.458 \\ 0.457 \end{bmatrix} \cdot 10^6,\ \boldsymbol{\lambda}'_{tt} = \begin{bmatrix} 0.011 \\ 0.006 \\ 1.007 \end{bmatrix} \cdot 10^9, \tag{37}$$

and their corresponding eigenvectors still constitute identity matrices.

It is noteworthy that the entries $\mathbf{K}_{tt}$ in both matrices (19) and $\mathbf{K}'_c$ are diagonal, in accordance with Eq. (27c), the coordinate frame axes indicate the principal directions of the translational stiffness. Moreover, as the off-diagonal elements in matrix $\mathbf{K}'_{rr}$ are much smaller than the diagonal ones, the diagonal elements are employed to approximate the principal rotational stiffnesses and the corresponding principal directions are considered as being parallel to the coordinate frame axes. As a result, the diagonal elements in $\mathbf{K}'_{rr}$ and $\mathbf{K}_{tt}$, denoted by τ_{xx}, τ_{yy}, τ_{zz} and σ_{xx}, σ_{yy}, σ_{zz}, respectively, are adopted to represent the principal rotational and translational stiffnesses.

Figure 9 shows the isocontours of the principal stiffnesses throughout the RWS of the two alternative Biglide parallel manipulators. It is observed that these two machines have significantly higher translational stiffness σ_{zz} in z-direction, two and three orders of magnitude larger than σ_{xx} and σ_{yy}, respectively. The translational stiffness σ_{yy} in the y-direction, being the smallest translational stiffness, remains constant as expressed by the element K_{55} of matrix (18). It should be noted that these two alternative machines have equivalent translational stiffness in x-direction, as displayed in Fig. 9(d), since the stiffness in this direction is subject to the only actuation stiffness. In addition, the rotational stiffness τ_{yy} about y-direction is one order of magnitude larger than the other two rotational stiffnesses. The rotational stiffnesses τ_{xx} and τ_{zz} of the original Biglide machine have common values at $z = 354$ mm, while the intersection occurs at $z = 356$ mm for the alternative one. Moreover, the principal stiffnesses except τ_{xx} and σ_{yy} becomes smaller with the increasing z-coordinates.

The relative difference of the principal stiffness between the two alternative Biglide grinders is defined as $\delta = (k - k')/k \cdot 100\%$, where k and k' stand for the stiffness of the original and

https://doi.org/10.1017/S0263574716000059 Published online by Cambridge University Press

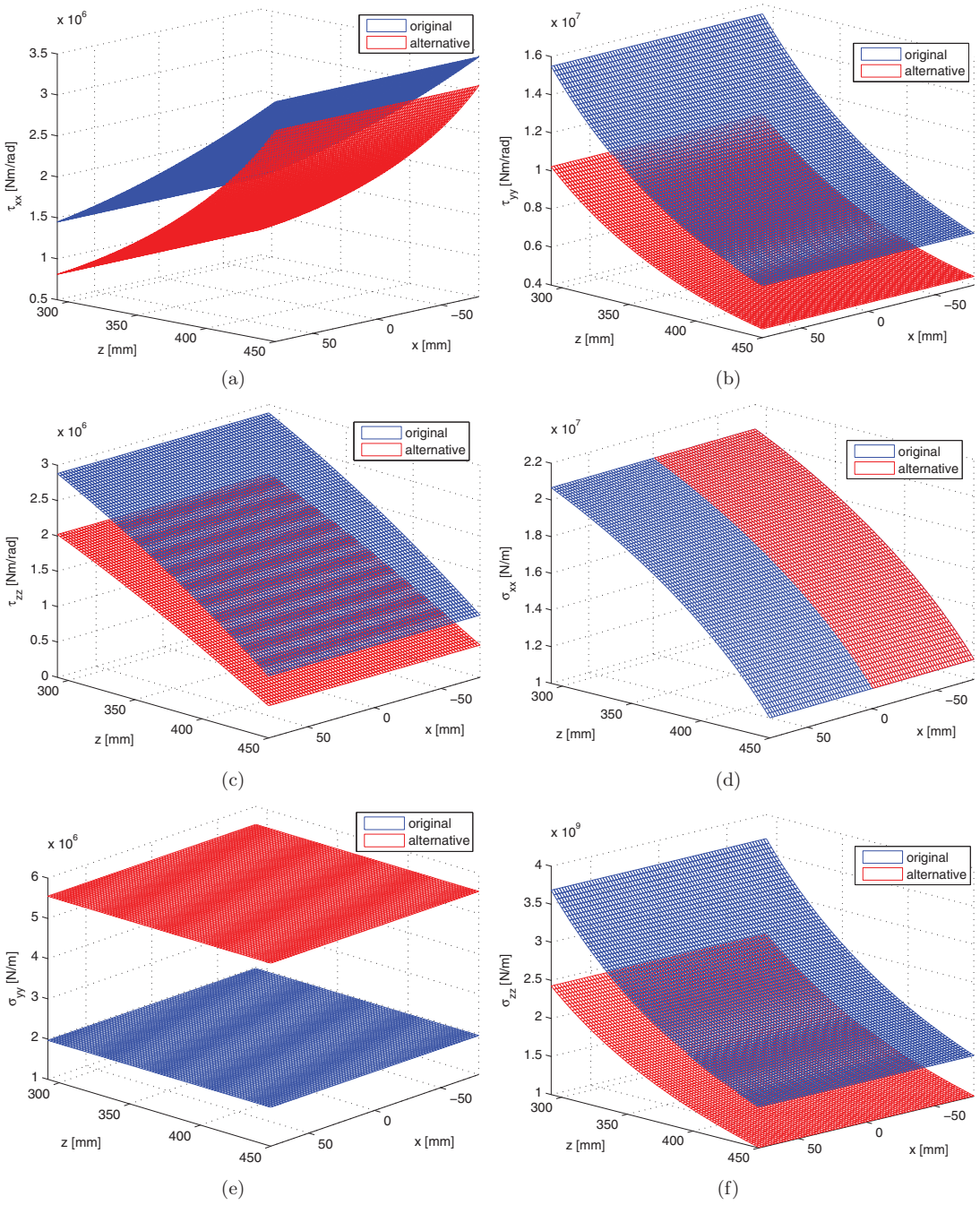


Fig. 9. Stiffness comparison of the two alternative Biglide parallel grinders.

alternative machines, respectively. As a consequence, the mean differences are calculated as displayed in Fig. 10. Compared to the alternative manipulator, the stiffnesses τ_{xx}, τ_{yy}, τ_{zz} and σ_{zz} of the original one increases by 30–40%. On the other hand, the alternative parallelogram in Fig. 7 significantly enhances the translational stiffness of the manipulator in y-direction, which increases by 180%.

With regard to the application of the Biglide parallel grinder, all the stiffness demonstrated in Fig. 9 are sufficient for the grinding process, since grinding does not require relative large force, differing from other material removal processing, such as milling. Therefore, in comparison with the original grinder, although the structural complexity of the alternative structure increases due to the universal joints, the modification can make the part of the parallel mechanism of the machine

https://doi.org/10.1017/S0263574716000059 Published online by Cambridge University Press

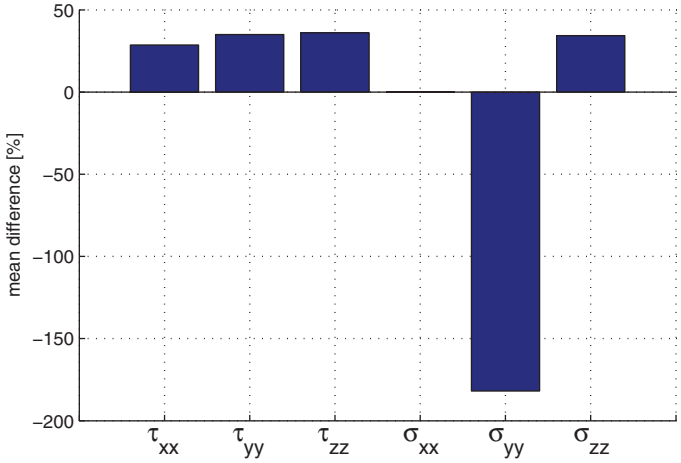


Fig. 10. The mean differences of the stiffness of the two alternative Biglide parallel grinders.

tool be lightweight and have lower inertia, but still guarantees high structural stiffness, particularly, the increased out-of-plane translational stiffness. The comparative study reveals that the stiffness in the direction of the normal to the plane of parallel mechanism's motion of the original Biglide machine can be effectively improved by assembling the two lower chains of the parallelogram in Fig. 5 in the shape of trapezoid, which can be used as a machine tool in material machining, such as milling.

On the other hand, in view of the elements in the Cartesian stiffness matrices of both manipulators, it is observed that the orders of some elements are much higher than those of the others, which implies that this will introduce some possible difficulties in the identification of the elastic parameters in the stiffness matrix.[29] For instance, the compliance matrix of stiffness matrix (29) is expressed as

$$\mathbf{C} = \mathbf{K}_c^{-1} = \begin{bmatrix} 7.012 & 0 & -0.004 & 0 & -1.004 & 0 \\ 0 & 0.645 & 0 & 0.058 & 0 & -0.001 \\ -0.004 & 0 & 3.469 & 0 & 0.007 & 0 \\ 0 & 0.058 & 0 & 0.489 & 0 & 0 \\ -1.004 & 0 & 0.007 & 0 & 5.220 & 0 \\ 0 & -0.001 & 0 & 0 & 0 & 0.003 \end{bmatrix} \cdot 10^{-7}. \tag{38}$$

Compared to the remaining non-zero elements, the compliance elements $c_{13} = c_{31}$, $c_{26} = c_{62}$, $c_{35} = c_{53}$ and c_{66} of $\mathbf{C}$ are much smaller, which leads to low identification accuracy.[29] Similarly, the compliance matrix at point $P2$ can be computed, while the magnitudes of the elements $c_{35} = c_{53}$ significantly increase. By observing the compliance matrices at points $P1$ and $P2$ and recalling to the isocontours of the principal stiffnesses in Fig. 9, the off-diagonal and the sixth diagonal elements of the compliance matrices of the both manipulators will encounter the problems of low accuracy in the parameter identification.

7. Validation of the Stiffness Model

In order to validate the stiffness models, the foregoing built analytical models are compared with FEA based evaluations, respectively. For instance, Fig. 11 displays the FE model of the alternative Biglide manipulator in Ansys/Workbench. The diagonal elements, c_{ii}, $i = 1, \ldots, 6$, of the compliance matrices $\mathbf{K}_c^{-1}$ of the two manipulators at points $P1$ and $P2$, are obtained from the FEA and analytical models, respectively. From the comparison of Table III, the compliance elements from the analytical model are close to those from FEA. The root-mean-squared (RMS) relative errors between the FEA and analytical models of the original manipulator at points $P1$ and $P2$ are 6.68% and 5.92%, respectively, and the RMS errors of the alternative one are 9.06% and 7.45%, which means the computation accuracies of the analytical models are acceptable. It is noted that the relative errors of

https://doi.org/10.1017/S0263574716000059 Published online by Cambridge University Press

Table III. Comparison of the diagonal elements of the compliance matrices for the Biglide manipulators.

	Original				Alternative			
	P1		P2		P1		P2	
	FEA	analy.	FEA	analy.	FEA	analy.	FEA	analy.
$c_{11} \cdot 10^{-6}$ (rad/Nm)	0.760	0.701	0.318	0.300	87.263	81.333	88.258	79.898
$c_{22} \cdot 10^{-6}$ (rad/Nm)	0.070	0.064	0.161	0.148	0.111	0.099	0.249	0.236
$c_{33} \cdot 10^{-6}$ (rad/Nm)	0.376	0.347	1.146	1.135	0.515	0.495	2.264	2.190
$c_{44} \cdot 10^{-6}$ (m/N)	0.052	0.049	0.090	0.090	0.056	0.049	0.105	0.090
$c_{55} \cdot 10^{-6}$ (m/N)	0.561	0.522	0.553	0.523	11.917	11.413	26.670	26.388
$c_{66} \cdot 10^{-10}$ (m/N)	2.738	2.717	7.177	6.539	4.697	4.122	10.273	9.928

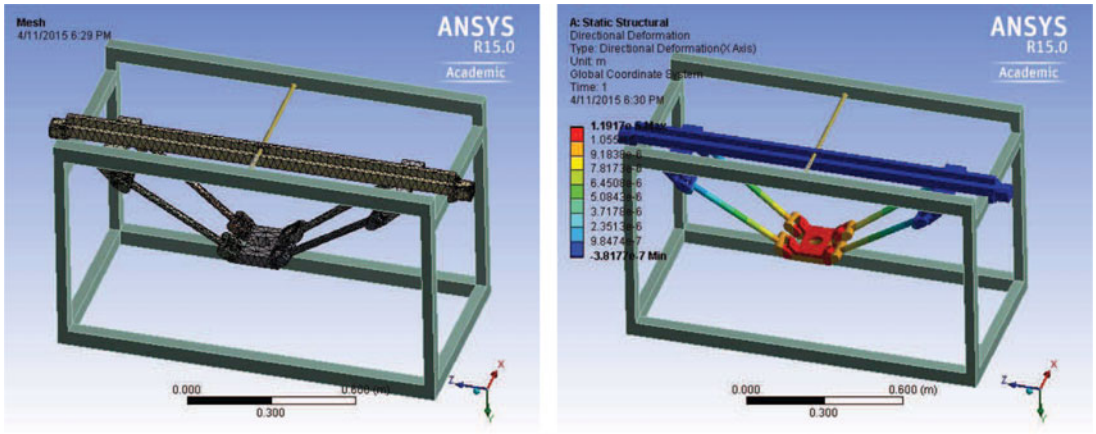


Fig. 11. FEA analysis of the alternative Biglide parallel manipulator at point $P1$: (a) meshed model; (b) deflection along the normal to the parallel mechanism's motion under unit force.

the alternative manipulator are larger than the those of the original one, wherein the reason is that the alternative one has more non-uniform beams and joints due to the universal joints, as this is a major reason causing the differences between the FEA and analytical models.

Based on the comparison, it is found that the difference between the analytical model and the FEA results is small and acceptable, which means that the developed stiffness model can effectively predict the manipulator stiffness.

8. Conclusions

This paper presents the comparative study of a Biglide parallel grinder with two alternative modular parallelograms with respect to the stiffness performances. The Cartesian stiffness matrices for these two machines are modeled, respectively, which turns out to have the property of being decoupled into two homogeneous translational and rotational stiffness sub-matrices. Resorting to the eigenvalue problem, the principal stiffnesses and the corresponding directions are identified to evaluate the translational and rotational stiffnesses of the manipulator either at a given pose or the overall WS. The isocontours of the principal stiffnesses over the RWS are visualized to show an image of the stiffness property. Moreover, the off-diagonal and the sixth elements of the compliance matrix of both manipulators will result in low accuracy of parameter identification due to their relatively small magnitudes.

The stiffness comparison between the original and alternative Biglide machines shows that the alternative parallelogram structure can make the machine tool be lightweight and have lower inertia,

https://doi.org/10.1017/S0263574716000059 Published online by Cambridge University Press

but still guarantees high structural stiffness, particularly, the enhanced out-of-plane translational stiffness. Moreover, the comparative study reveals that the stiffness in the direction of the normal to the plane of parallel mechanism's motion of the original Biglide machine can be effectively improved by assembling the two lower chains of the parallelogram in the shape of trapezoid, which allows the manipulator to be developed as a machine tool for material machining. In the future, optimum design on the geometric and structural parameters will be carried out towards lightweight design and high dynamic behaviors.

References

1. J.-P. Merlet, *Parallel Robots* (Kluwer Academic Publishers, Norwell, MA, USA, 2000).
2. C. Gosselin, "Stiffness mapping for parallel manipulators," *IEEE Trans. Robot. Autom.* **6**(3), 377–382 (1990).
3. S.-F. Chen and I. Kao, "Conservative congruence transformation for joint and Cartesian stiffness matrices of robotic hands and fingers," *Int. J. Robot. Res.* **19**, 835–847 (2000).
4. G. Alici and B. Shirinzadeh, "Enhanced stiffness modeling, identification and characterization for robot manipulators," *IEEE Trans. Robot.* **21**(4), 554–564 (2005).
5. C. Quennouelle and C. Gosselin, "Stiffness Mtrix of Compliant Parallel Mechanisms," *Advances in Robot Kinematics: Analysis and Design* (Springer, Netherlands, 2008) pp. 331–341.
6. C. Gosselin and D. Zhang, "Stiffness analysis of parallel mechanisms using a lumped model," *Int. J. Robot. Autom.* **17**(1), 17–27 (2002).
7. D. Zhang and C. Gosselin, "Parallel kinematic machine design with kinetostatic model," *Robotica* **4**(7), 429–438 (2002).
8. F. Majou, C. Gosselin, P. Wenger and D. Chablat, "Parametric stiffness analysis of the Orthoglide," *Mech. Mach. Theory* **42**(3), 296–311 (2007).
9. A. Pashkevich, D. Chablat and P. Wenger, "Stiffness analysis of overconstrained parallel manipulators," *Mech. Mach. Theory* **44**(5), 966–982 (2009).
10. A. Pashkevich, A. Klimchik and D. Chablat, "Enhanced stiffness modeling of manipulators with passive joints," *Mech. Mach. Theory* **46**(5), 662–679 (2011).
11. N. Ciblak and H. Lipkin, "Synthesis of Cartesian stiffness for robotic applications," *Proc. IEEE Int. Conf. Robot. Autom.* **3**, 2147–2152 (1999).
12. S. Huang and J. M. Schimmels, "The eigenscrew decomposition of spatial stiffness matrices," *IEEE Trans. Robot. Autom.* **16**(2), 146–156 (2000).
13. X. Ding and J. M. Selig, "On the compliance of coiled springs," *Int. J. Mech. Sci.* **46**(5), 703–727 (2004).
14. J. Dai and X. Ding, "Compliance analysis of a three-legged rigidly-connected platform device," *ASME J. Mech. Des.* **128**(4), 755–764 (2006).
15. G. Chen, H. Wang, Z. Lin and X. Lai, "The principal axes decomposition of spatial stiffness matrices," *IEEE Trans. Robot.* **31**(1), 191–207 (2015).
16. J. Kövecses and S. Ebrahimi, "Parameter analysis and normalization for the dynamics and design of multibody systems," *ASME J. Comput. Nonlin. Dyn.* **4**(3), 031008 (2009).
17. A. Taghvaeipour, J. Angeles and L. Lessard, "On the elastostatic analysis of mechanical systems," *Mech. Mach. Theory* **58**, 202–216 (2012).
18. J. Angeles, "On the nature of the Cartesian stiffness matrix," *Ingeniería Mecánica* **3**(5), 163–170 (2010).
19. P. Zou, "Kinematic analysis of a Biglide parallel grinder," *J. Mater. Process. Technol.* **138**(1–3), 461–463 (2003).
20. C. Germain, S. Caro, S. Briot and P. Wenger, "Singularity-free design of the translational parallel manipulator IRSBot-2," *Mech. Mach. Theory* **64**, 262–285 (2013).
21. K. Nagai and Z. Liu, "A Systematic Approach to Stiffness Analysis of Parallel Mechanisms," *Proc. IEEE Int. Conf. Robot. Autom.*, Pasadena, California, USA (2008) pp. 1543–1548.
22. G. Wu, S. Bai and J. Kepler, "Mobile platform center shift in spherical parallel manipulators with flexible limbs," *Mech. Mach. Theory* **75**, 12–26 (2014).
23. D. Wang, R. Fan and W. Chen, "Stiffness analysis of a hexaglide parallel loading mechanism," *Mech. Mach. Theory* **70**, 454–473 (2013).
24. J. E. Shigley, C. R. Mischke and T. H. Brown, *Standard Handbook of Machine Design* (McGraw-Hill, New York, USA, 2004).
25. R. G. Roberts, "On the Normal Form of a Spatial Stiffness Matrix," *Proc. IEEE Int. Conf. Robot. Autom.*, Washington, DC, USA, vol. 1 (2002) pp. 556–561.
26. J. Angeles, *Fundamentals of Robotic Mechanical Systems: Theory, Methods, and Algorithms* (Springer, New York, 2007).
27. G. Strang, *Linear Algebra and Its Applications*, 4th ed. (Cengage Learning, Boston, MA, USA, 2005).
28. S. Briot, A. Pashkevich and D. Chablat, "Optimal Technology-Oriented Design of Parallel Robots for High-Speed Machining Applications," *Proc. IEEE Int. Conf. Robot. Autom.*, Anchorage, Alaska (2010) pp. 1155–1161.

https://doi.org/10.1017/S0263574716000059 Published online by Cambridge University Press

29. A. Klimchik, B. Furet, S. Caro and A. Pashkevich, "Identification of the manipulator stiffness model parameters in industrial environment," *Mech. Mach. Theory* **90**, 1–22 (2015).

Appendix A

The non-zero elements of the Cartesian stiffness matrix (18) are given by

$$K_{11} = 6k_{11}C_q^2 + (6k_{33} + k_{44}d^2 + 2k_{35}hC_q + 3k_{55}h^2C_q^2)S_q^2 \tag{A1a}$$

$$K_{13} = k_{35}hS_qC_{2q} + \frac{1}{4}k_{55}hS_{2q}(2r - 3hC_{2q}) \tag{A1b}$$

$$K_{15} = -(6k_{35} + k_{55}hC_q)S_q \tag{A1c}$$

$$K_{22} = 2K_ar^2C_q^3S_q^{-2} + \frac{3}{2}k_{44}(h^2S_q^4 + 4r^2)S_q^{-2} \tag{A1d}$$

$$K_{24} = -2K_arC_q^2S_q^{-1} \tag{A1e}$$

$$K_{26} = k_{44}h \tag{A1f}$$

$$K_{33} = 6k_{11}S_q^2 + (6k_{33} + k_{44}d^2)C_q^2 - 2k_{35}C_q(6r - hC_q^2) + k_{55}\left[\frac{3}{8}h^2(C_{4q} + 3) + 6r^2 + 2hrC_q^2\right] \tag{A1g}$$

$$K_{35} = -k_{55}hS_q^2 \tag{A1h}$$

$$K_{44} = 2K_aC_q \tag{A1i}$$

$$K_{55} = 6k_{55} \tag{A1j}$$

$$K_{66} = (2K_aC_q^3 + 6k_{44})S_q^{-2} \tag{A1k}$$

https://doi.org/10.1017/S0263574716000059 Published online by Cambridge University Press